Wind Power Smoothing Control by Energy Storage Based on Area-equilibrium Empirical Mode Decomposition

Yu-Qing Bao, *Senior Member*, *IEEE*, Qing-Quan Yu, Yu Chen, and Shu-Han Yu

***Abstract*—Energy storage can smooth the fluctuations of wind power integrated into the grid. Due to the strong adaptability of the empirical mode decomposition (EMD) algorithm to non-stationary signals, it is widely used in wind power smoothing control strategies. However, traditional EMD algorithms cannot guarantee that the upper and lower areas of the calculated intrinsic mode functions (IMFs) are equal, which tends to result in imbalanced calculated energy storage power and thus exceeding the limit of energy storage capacity. Focusing on wind power smoothing control by energy storage, this paper proposes a strategy based on the area-equilibrium EMD, which modifies the upper and lower areas of the IMFs to achieve a more balanced distribution. As a result, the IMFs contain less energy, and consequently, the energy contained in the calculated smoothing power is also reduced. This makes the energy storage capacity less likely to exceed the limit, thereby achieving better wind power smoothing performance under given energy storage capacity. Case studies show that the proposed strategy results in more balanced upper and lower areas of the IMFs, reduces the fluctuating range of calculated energy storage, and improves the wind power smoothing effectiveness.**

***Index Terms*—Wind power, energy storage, empirical mode decomposition (EMD), fluctuation mitigation.**

I. INTRODUCTION

WITH the increasing penetration of renewable energy, the power fluctuations caused by renewable energy are growing. The inherent randomness and volatility of wind power pose significant challenges to the safe and stable operation of power systems during grid integration. According to the current national standards in China, wind farms are required to achieve continuous and smooth regulation of active power. Newly-constructed wind farms must be equipped with appropriate energy storage devices to ensure that the variations in active power of wind farms adhere to the requirements for the secure and stable operation of the power system [1]-[3].

Smoothing wind power fluctuations via energy storage is currently a prominent research focus. Energy storage systems (ESSs) encompass a wide range of technologies, including superconducting magnetic energy storage (SMES) [4], [5], battery energy storage [6], pumped storage [7], and hybrid energy storage [8]. The effectiveness and economic viability of ESSs in smoothing wind power fluctuations depend critically on the control strategies employed. Consequently, various effective wind power fluctuation smoothing strategies for ESSs are proposed.

In [4], the SMES is integrated into the wind farm system. The electrical energy can be injected into or supplied from the SMES coil, thereby mitigating the power fluctuation. In [5], the advantages of SMES are combined with the characteristics of application scenarios, and sliding mode variable structure control is introduced into the SMES, effectively smoothing wind power fluctuations. In [6], a strategy utilizing the rule-based ramp control strategy to charge/discharge the energy storage to compensate for the difference between actual power and desired power is presented to mitigate the wind power fluctuations. In [7], a droop-vector control strategy based on variable speed pumped storage system is proposed to smooth the wind power fluctuations. In [8], an improved low-pass filtering algorithm is proposed to achieve the power allocation between lithium battery and supercapacitor, which can effectively suppress the power fluctuations. Reference [9] proposes a coordination control method that utilizes a battery energy storage system (BESS) to mitigate wind power fluctuations. A flexible first-order low-pass filter with an optimized time constant is developed to limit the power fluctuations. Reference [10] presents a control method of the BESS based on the quasi-zero phase filter. It incorporates wind power forecast information into a sliding average filtering algorithm to construct a quasi-zero phase filter for smoothing control of the BESS. Reference [11] proposes a novel two-stage model predictive control scheme that effectively smooths the wind generation volatility by fully utilizing the ESS with distinct characteristics. Reference [12] proposes a new coordinated wind power smoothing control strategy for multi-wind turbines and ESSs. The strategy is based on a multi-agent deep reinforcement learning method and can further smooth wind power fluctuations. Reference [13] presents an online-wavelet based coordinated control strate-

Manuscript received: June 25, 2024; revised: September 19, 2024; accepted: October 29, 2024. Date of CrossCheck: October 29, 2024. Date of online publication: November 22, 2024.

This work was supported in part by the National Natural Science Foundation of China (No. 51707099).

Y.-Q. Bao (corresponding author), Q.-Q. Yu, Y. Chen, and S.-H. Yu are with Nanjing Normal University, Nanjing 210046, China (e-mail: baoyuqing@njnu.edu.cn; 2642610340@qq.com; 1014726201@qq.com; 2987059919@qq.com).

DOI: 10.35833/MPCE.2024.000674

gy that utilizes the wavelet multi-resolution signal decomposition to allocate fluctuations with different frequency bands to the lithium battery and the super capacitor. In [14], the wavelet decomposition based on wavelet packet is performed on wind power to obtain its components in each frequency band, and the local peak-shaving and valley-filling of the components are performed to smooth the power fluctuations. Reference [15] presents a novel robust dynamic-wavelet-enabled wind power smoothing approach considering the wind power uncertainty. It coordinates batteries and supercapacitors optimally, resulting in a high efficiency. In [16] and [17], a probabilistic forecasting-based sizing and control scheme for hybrid energy storage system (HESS) is proposed to cost-effectively smooth wind power fluctuations. It utilizes the complementary response characteristics of the HESS to suppress the fluctuating components.

Although the above methods have achieved effective results in smoothing wind power fluctuations, they only mitigate fluctuations at certain fixed frequencies within wind power. They struggle to capture non-stationary fluctuation characteristics across different frequencies [18], [19]. Empirical mode decomposition (EMD), however, can decompose signals with non-linear and non-stationary characteristics. It possesses adaptive advantages in characterizing wind power fluctuations and is therefore suitable for smoothing wind power fluctuations [20]-[22]. Regarding the wind power fluctuation smoothing method based on EMD, in [23], a method based on the improved EMD for hydrogen energy storage (HES) is proposed to suppress wind power fluctuation. An improved EMD is designed as a power allocation control method to maintain the charging-discharging balance of the HES. In [24], based on EMD, the original wind power signal is decomposed into power components that meet the grid-connected fluctuation limit and hybrid energy storage power tasks, which can satisfy the demand for stabilization and improve the economic efficiency of the system. In [25], a method based on the improved moving average and ensemble empirical mode decomposition (EEMD) is proposed to smooth wind power fluctuations. In [26], an improved power division method based on the complete ensemble empirical mode decomposition (CEEMD) and dynamic mode decomposition (DMD) is proposed, where CEEMD is used to decompose the intrinsic mode function (IMF) of the remaining fluctuations. Reference [27] adopts the instantaneous complete ensemble empirical mode decomposition with adaptive noise (ICEEMDAN) strategy to achieve real-time decomposition of the energy storage power, facilitating internal power distribution within the HESS.

Existing wind power smoothing control strategies using energy storage are listed in Table I. It can be observed that the wavelet analysis [13]-[15], variational mode decomposition (VMD) [16], [17], and EMD [23]-[27] are all based on signal decomposition. However, existing strategies cannot guarantee that the fluctuating power decomposed equals the area enclosed with the time axis, leading to the following two problems.

1) Continuous energy changes. Since the area enclosed by the fluctuating power and the time axis reflects the energy contained in the fluctuating power, inequality in the upper and lower areas may lead to continuous increase or decrease in energy.

2) Increased demand for energy. Since the amount of energy stored in an ESS is limited, continuous increase or decrease in energy results in reaching its state of charge (SOC) limits. When SOC limits are reached, the ESS will not be able to output or absorb power, seriously affecting the smoothing control of wind power fluctuations.

TABLE I
WIND POWER SMOOTHING CONTROL STRATEGIES USING ENERGY STORAGE

Control strategy	Based on signal decomposition	Balanced upper and lower areas of IMFs
Low-pass filtering algorithm [8]-[10]	×	×
Model predictive control [11]	×	×
Reinforcement learning [12]	×	×
Wavelet analysis [13]-[15]	√	×
VMD [16], [17]	√	×
EMD [23]-[27]	√	×
Proposed	√	√

To address these issues, this paper proposes a strategy based on the area-equilibrium EMD algorithm, which uses an area-equilibrium method to make the upper and lower areas of each IMF as equal as possible, thereby reducing the dependence of energy storage on power for smoothing wind power fluctuations and using less energy to smooth more wind power fluctuations.

The remainder of this paper is organized as follows. Section II presents the EMD-based wind power smoothing control strategy and its existing problems. Section III proposes the area-equilibrium EMD algorithm for the wind power smoothing control by the energy storage. Section IV provides case studies, and Section V concludes this paper.

II. EMD-BASED WIND POWER SMOOTHING CONTROL STRATEGY AND ITS EXISTING PROBLEMS

A. EMD-based Wind Power Smoothing Control Strategy

The overall block diagram of the EMD-based wind power smoothing control strategy is shown in Fig. 1. To achieve the smoothing of wind power, the original wind power $P_W(t)$ is collected and used as the input signal for EMD, resulting in several IMFs and a residue. Then, the ESS power adjustment command $P_{ESS}(t)$ is calculated using the IMFs. Based on this, ESS control is carried out, resulting in the filtered wind power.

The specific steps are as follows.

1) Represent the original wind power $P_W(t)$ as the initial input signal $x(t)$.

2) Compute the EMD of signal $x(t)$, which results in several IMFs $c_i(t)$ and the residual signal $r_n(t)$, as follows:

$$x(t)=\sum_{i=1}^{n}c_i(t)+r_n(t) \tag{1}$$

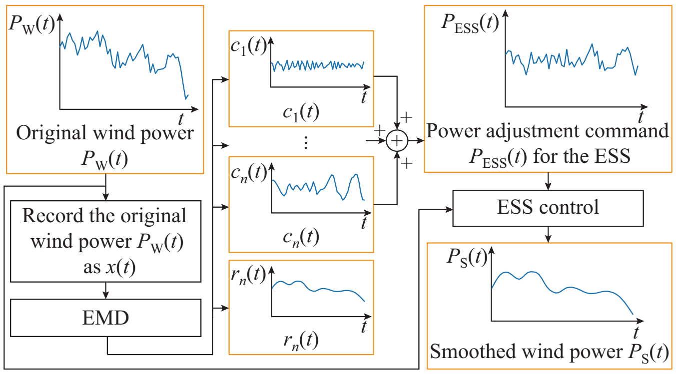

Fig. 1. Overall block diagram of EMD-based wind power smoothing control strategy.

where $c_i(t)$ is the i^{th} IMF; and $r_n(t)$ is the n^{th} residual signal.

This can be achieved through the following process.

Step 1: find all local extremal (maximal or minimal) points in the signal $x(t)$ and connect them (with cubic spline or Hermite interpolation) to form upper and lower envelope lines, respectively, denoted as $H(t)$ and $L(t)$.

Step 2: compute the mean curve $m(t)$ of $H(t)$ and $L(t)$ as:

$$m(t)=\frac{H(t)+L(t)}{2} \tag{2}$$

Step 3: subtract $m(t)$ from $x(t)$ to obtain a candidate IMF, denoted as $h(t)$.

$$h(t)=x(t)-m(t) \tag{3}$$

Step 4: if $h(t)$ is an IMF, terminate the process; otherwise, treat $h(t)$ as the new signal $x(t)$ and repeat *Steps 1-3* until $h(t)$ becomes an IMF, denoted as $c_i(t)$.

Step 5: subtract the identified IMF $c_i(t)$ from $x(t)$ to obtain the residue:

$$r_i(t)=x(t)-c_i(t) \tag{4}$$

An example of the original curve of $x(t)$ and the corresponding curves of $H(t)$, $L(t)$, $m(t)$, $c_i(t)$, and $r_i(t)$ are shown in Fig. 2(a) and (b). It can be observed that $c_i(t)$ represents the fluctuating component of $x(t)$.

Step 6: repeat *Steps 1-5* until the residual signal $r_n(t)$ satisfies the smoothing requirement for wind power $P_W(t)$.

3) Compute the sum of IMFs as the reference power control signal for energy storage:

$$P_{ESS}(t)=\sum_{i=1}^{n}c_i(t) \tag{5}$$

Then, the power adjustment command $P_{ESS}(t)$ can be sent to the ESS through open-loop or closed-loop control.

B. Problems with Traditional EMD Algorithm

The implementation of EMD as an algorithm for adaptive data processing in nonlinear and non-stationary time series was first presented in [28]. The traditional EMD algorithm can decompose the original wind power $P_W(t)$ into IMFs and use the obtained IMFs to construct the power adjustment command $P_{ESS}(t)$ required for energy storage. However, the application of EMD algorithm in the field of energy storage has the following key problems.

1) The EMD algorithm can obtain IMFs of different time scales, but it cannot guarantee that the upper and lower areas of each IMF are equal, as shown in Fig. 2(b). Unequal IMF areas for power signals imply a continuous increase or decrease in energy, as shown in Fig. 2(c).

2) Since the amount of energy stored in an ESS is limited, continuous increase or decrease in energy results in reaching its SOC limits. When SOC limits are reached, the ESS will not be able to output or absorb power, seriously affecting the smoothing control of wind power fluctuations.

To address these issues, a wind power smoothing control strategy based on the area-equilibrium EMD algorithm is proposed.

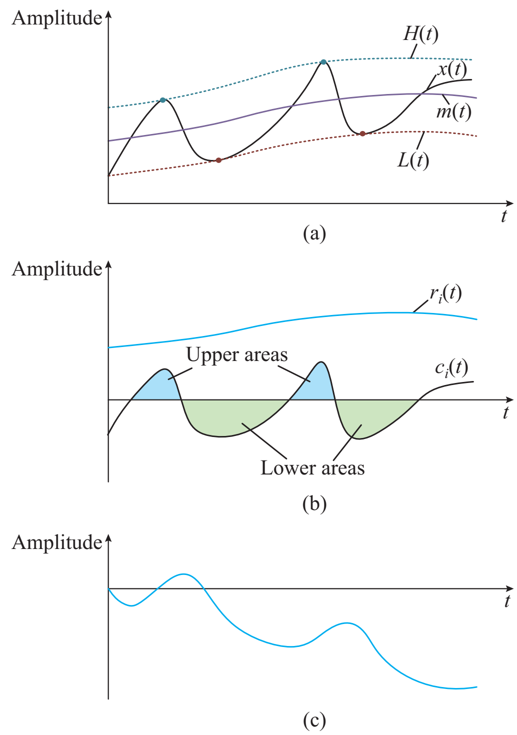

Fig. 2. An example of EMD signal decomposition. (a) Curves of $x(t)$, $H(t)$, $L(t)$, and $m(t)$. (b) Curves of $c_i(t)$ and $r_i(t)$. (c) Energy (integral) of $c_i(t)$.

III. Area-equilibrium EMD Algorithm

A. Overall Structure of Proposed Strategy

The key to the proposed strategy is the calculation of the equilibrium of the upper and lower areas for each IMF. Figure 3 shows the flowchart of the proposed strategy. It can be observed that the area-equilibrium method is embedded within the EMD algorithm. The purpose of the area-equilibrium method is to balance the upper and lower areas of the IMF curves $c_i(t)$ computed by the EMD algorithm to calculate a more evenly equilibrious curve $c_i'(t)$. By this way, the corresponding energy of power adjustment command $P_{ESS}(t)$ can be lowered.

In the area-equilibrium method, the first step is to calculate the extreme points and zero-crossing times of $c_i(t)$, based on which the upper and lower areas are calculated. Then, according to the area balancing requirement, the intersection points $(\Delta c_{i,k}, t'_{s,k})$ of the new dividing line $b_i(t)$ and

$c_i(t)$ are calculated, and a cubic spline or Hermite interpolation is used to obtain the dividing line $b_i(t)$. Finally, the modified IMF curve $c_i'(t)$ is obtained by subtracting $b_i(t)$ from $c_i(t)$.

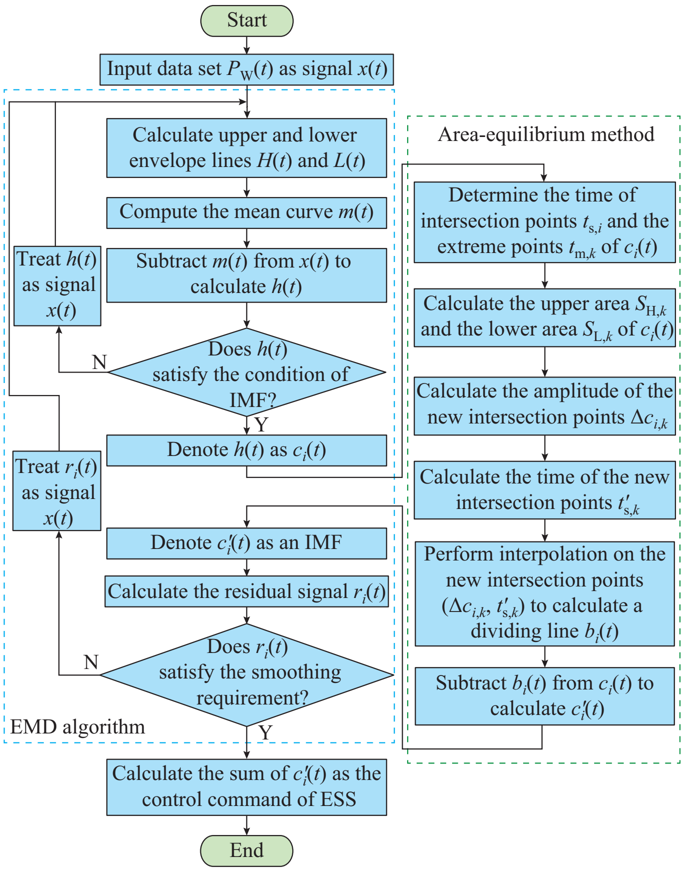

Fig. 3. Flowchart of proposed strategy.

B. Calculation of Upper and Lower Areas

The purpose of calculating the upper and lower areas of the IMF curve $c_i(t)$ is to find a basis of the area-equilibrium processing. Since the adjustment of $c_i(t)$ has different magnitudes at different positions, the calculation of the upper and lower areas also needs to be segmented.

Figure 4(a) illustrates an example of segmented upper and lower areas. The IMF curve is denoted as $c_i(t)$, the time corresponding to the intersection points between $c_i(t)$ and the t-axis is denoted as $t_{s,k}$, and time corresponding to the k^{th} and $(k+1)^{\text{th}}$ extreme points of $c_i(t)$ is denoted as $t_{m,k}$ and $t_{m,k+1}$, respectively. These intersection points and extreme points enclose the k^{th} segmented upper area $S_{H,k}$ and the k^{th} segmented lower area $S_{L,k}$ of $c_i(t)$. The upper area $S_{H,k}$ and the lower area $S_{L,k}$ can be calculated by:

$$S_{H,k}=\int_{t_{s,k}}^{t_{m,k+1}} c_i(t)\mathrm{d}t \tag{6}$$

$$S_{L,k}=\int_{t_{m,k}}^{t_{s,k}} (-c_i(t))\mathrm{d}t \tag{7}$$

However, (6) and (7) only suit for continuous forms of $c_i(t)$. Real sampled data are discrete and therefore require discretization of (6) and (7).

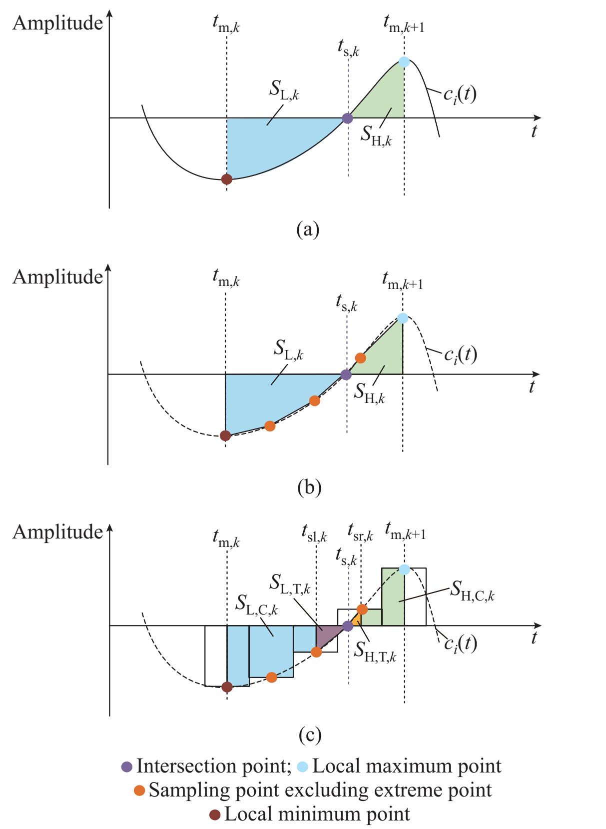

Fig. 4. An example of upper and lower area calculation. (a) Segmented upper and lower areas of $c_i(t)$. (b) Piecewise-linearized areas. (c) Equivalent segmented block areas.

Figure 4(b) shows the piecewise-linearized areas of $c_i(t)$ under discrete sampling, and Fig. 4(c) illustrates the equivalent segmented block areas. From Fig. 4(c), it can be observed that both the upper and lower areas contain a set of bar-shaped areas $S_{H,C,k}$, $S_{L,C,k}$, as well as triangular areas $S_{H,T,k}$, $S_{L,T,k}$ close to the zero-crossing point.

$$S_{H,k}=S_{H,C,k}+S_{H,T,k} \tag{8}$$

$$S_{L,k}=S_{L,C,k}+S_{L,T,k} \tag{9}$$

The bar-shaped areas $S_{H,C,k}$, $S_{L,C,k}$ are determined by each sampling point and can be calculated using the discrete trapezoidal integration formula:

$$S_{H,C,k}=\left(\frac{c_i(t_{sr,k})}{2}+c_i(t_{sr,k}+\Delta t)+\ldots+\frac{c_i(t_{m,k+1})}{2}\right)\Delta t \tag{10}$$

$$S_{L,C,k}=-\left(\frac{c_i(t_{m,k})}{2}+c_i(t_{m,k}+\Delta t)+\ldots+\frac{c_i(t_{sl,k})}{2}\right)\Delta t \tag{11}$$

where $t_{sl,k}$ and $t_{sr,k}$ are the previous and subsequent sampling points before and after the zero-crossing point of $c_i(t)$, respectively; and Δt represents the step size of the sampling.

The triangular areas $S_{H,T,k}$, $S_{L,T,k}$ are enclosed by the nearest sampling point to the zero-crossing point and the zero-crossing point itself. The zero-crossing point $t_{s,k}$ can be calculated as:

$$t_{s,k}=t_{sl,k}-\frac{c_i(t_{sl,k})}{c_i(t_{sr,k})}\Delta t \tag{12}$$

Based on (12), the triangular areas can be calculated as:

$$S_{H,T,k}=\frac{(t_{sr,k}-t_{s,k})c_i(t_{sr,k})}{2} \tag{13}$$

$$S_{L,T,k}=-\frac{(t_{s,k}-t_{sl,k})c_i(t_{sl,k})}{2} \tag{14}$$

Formulas (8)-(14) constitute the algorithm for calculating the upper and lower areas.

C. Calculation of Modified IMF Curve

To make the upper area $S_{H,k}$ and the lower area $S_{L,k}$ as equal as possible, these two areas need to be re-segmented. Assuming the new dividing line is at a distance of $\Delta c_{i,k}$ below the t-axis, the upper and lower areas determined by the new dividing line can be represented as $S'_{H,k}$ and $S'_{L,k}$, respectively:

$$S'_{H,k}=S_{H,k}+\Delta S_{H,k} \tag{15}$$

$$S'_{L,k}=S_{L,k}-\Delta S_{L,k} \tag{16}$$

where $\Delta S_{H,k}$ and $\Delta S_{L,k}$ represent the decrease and increase in the upper and lower areas due to the new dividing line, respectively. $\Delta S_{H,k}$ and $\Delta S_{L,k}$ can be estimated as:

$$\Delta S_{H,k}\approx\int_{t'_{s,k}}^{t_{s,k}}(c_i(t)+\Delta c_{i,k})\mathrm{d}t+(t_{m,k+1}-t_{s,k})\Delta c_{i,k} \tag{17}$$

$$\Delta S_{L,k}\approx(t'_{s,k}-t_{m,k})\Delta c_{i,k}+\int_{t'_{s,k}}^{t_{s,k}}(-c_i(t))\mathrm{d}t \tag{18}$$

The purpose of re-segmentation is to make the new obtained upper and lower areas $S'_{H,k}$ and $S'_{L,k}$ equal, i.e.,

$$S'_{H,k}=S'_{L,k} \tag{19}$$

Substituting (15) and (16) into (19) yields:

$$S_{H,k}+\Delta S_{H,k}=S_{L,k}-\Delta S_{L,k} \tag{20}$$

By introducing (17) and (18) into (20), the value of $\Delta c_{i,k}$ can be derived as:

$$\Delta c_{i,k}=\frac{S_{L,k}-S_{H,k}}{t_{m,k+1}-t_{m,k}} \tag{21}$$

Then, the time of the new intersection point $t'_{s,k}$ can be calculated as:

$$t'_{s,k}\approx t_{s,k}-\frac{\Delta c_{i,k}}{\dot{c}_i(t_{s,k})} \tag{22}$$

where $\dot{c}_i(t_{s,k})$ is the derivative of $c_i(t)$ at time $t_{s,k}$.

Once $\Delta c_{i,k}$ and $t'_{s,k}$ are calculated, the position of the new intersection point can be expressed by $(\Delta c_{i,k}, t'_{s,k})$. After all the intersection points are calculated, the dividing line $b_i(t)$ can be obtained by performing cubic spline or Hermite interpolation on all intersection points, as shown in Fig. 5(a). After $b_i(t)$ is determined, the modified IMF curve $c'_i(t)$ can be finally obtained by subtracting $b_i(t)$ from $c_i(t)$, as shown in Fig. 5(b). After modification, the upper and lower areas of the modified IMF curve $c'_i(t)$ are approximately balanced.

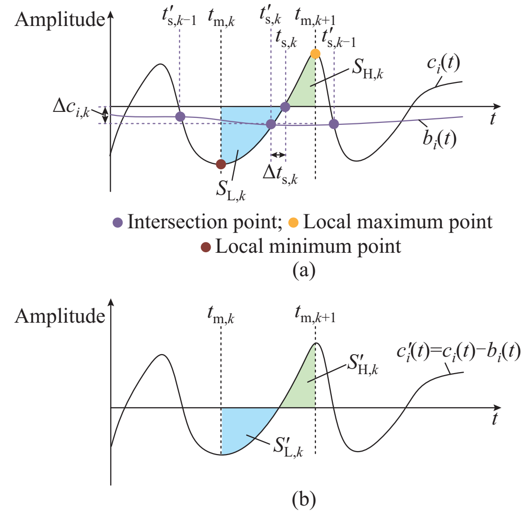

Fig. 5. An example of calculating modified IMF curve $c'_i(t)$. (a) Calculation of dividing line $b_i(t)$. (b) Finally obtained $c'_i(t)$.

IV. Case Study

A. Performance of Area-equilibrium EMD Algorithm on Signal Decomposition

In this subsection, the proposed algorithm is applied to signal decomposition, so as to verify its effectiveness in balancing the upper and lower areas of the IMFs.

Figure 6 presents a simulated wind power curve $x(t)$, which is taken as the input signal for the proposed algorithm.

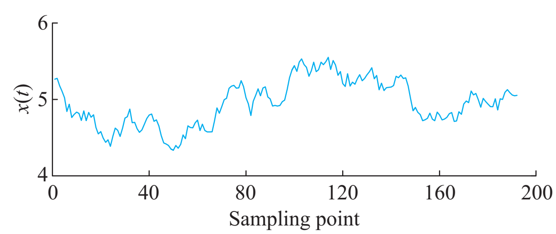

Fig. 6. Simulated wind power curve $x(t)$.

Assuming the signal is decomposed into two layers, two IMFs $c_1(t)$ and $c_2(t)$ are obtained, respectively, and a residue $r_2(t)$ can also be obtained by subtracting $c_1(t)$ and $c_2(t)$ from $x(t)$. The input signal $x(t)$ is decomposed by using the proposed algorithm and compared with the traditional EMD algorithm, as shown in Figs. 7-9. Figures 7 and 8 present the comparison of $c_1(t)$, $c_2(t)$ and probability distributions of their integrals before and after modification using the proposed algorithm. Figure 9 illustrates the overall trends of the decomposed $c_1(t)$, $c_2(t)$, and $r_2(t)$ between the two algorithms. From Figs. 7-9, it can be observed that:

1) The modified IMFs have more balanced areas. Figures 7 and 8 illustrate that the modified IMFs (curves of $c'_1(t)$ and $c'_2(t)$) display more balanced upper and lower distributions compared with their unmodified counterparts (curves of $c_1(t)$ and $c_2(t)$). The integrals of $c'_1(t)$ and $c'_2(t)$ are smaller compared to $c_1(t)$ and $c_2(t)$, indicating that $c'_1(t)$ and $c'_2(t)$ contain less energy. This results in lower energy consumption corresponding to the energy storage power.

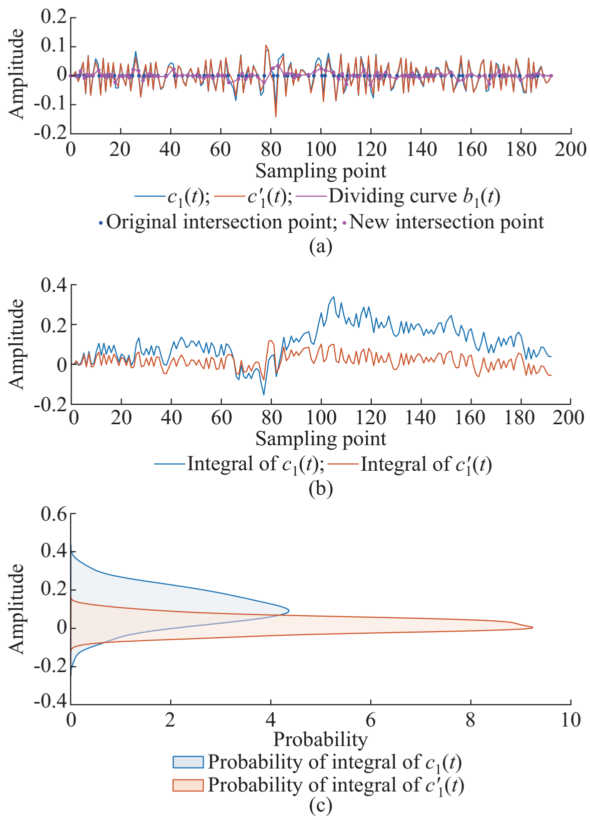

Fig. 7. Calculation of modified IMF curve $c_1'(t)$. (a) IMF curve $c_1(t)$ versus modified IMF curve $c_1'(t)$. (b) Integral of $c_1(t)$ versus integral of $c_1'(t)$. (c) Probability of integral of $c_1(t)$ versus probability of integral of $c_1'(t)$.

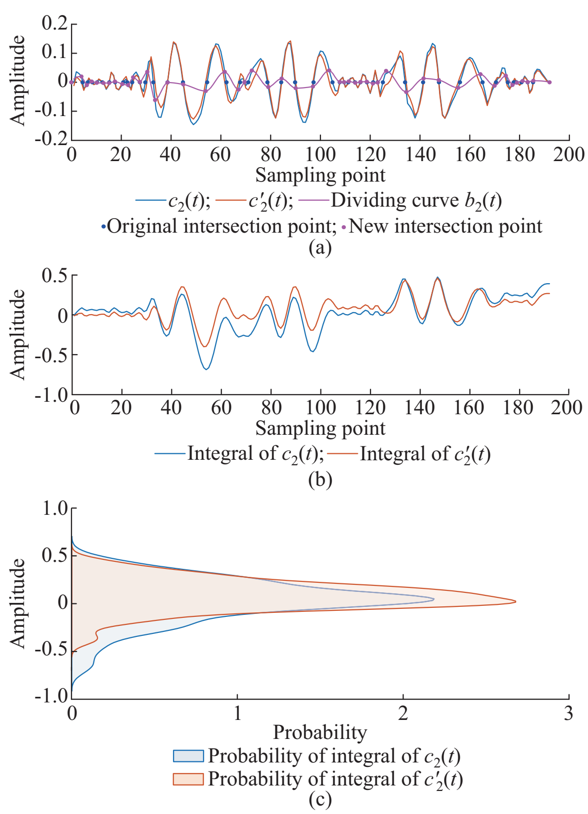

Fig. 8. Calculation of modified IMF curve $c_2'(t)$. (a) IMF curve $c_2(t)$ versus modified IMF curve $c_2'(t)$. (b) Integral of $c_2(t)$ versus integral of $c_2'(t)$. (c) Probability of integral of $c_2(t)$ versus probability of integral of $c_2'(t)$.

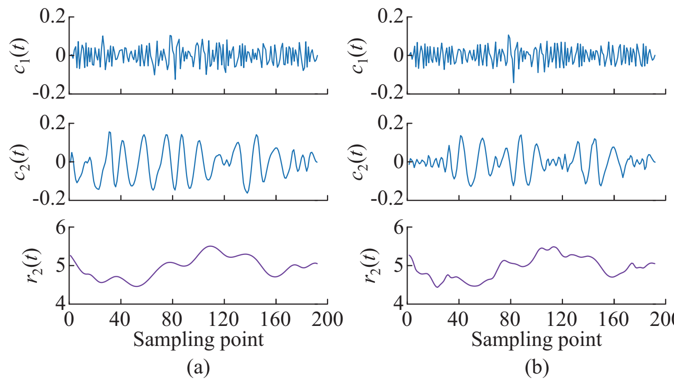

Fig. 9. Decomposition results by traditional EMD algorithm and proposed algorithm. (a) Traditional EMD algorithm. (b) Proposed algorithm.

2) Differences in decomposition results. From Fig. 9, it can be observed that the IMFs $c_1'(t)$, $c_2'(t)$, and residual $r_2(t)$ obtained by the proposed algorithm differ from those obtained by the traditional EMD algorithm. On the one hand, the IMFs $c_1'(t)$ and $c_2'(t)$ obtained by the proposed algorithm have smaller amplitudes compared with those of the traditional EMD algorithm, and their upper and lower areas are more balanced. On the other hand, the residual $r_2(t)$ of the proposed algorithm fluctuates more compared with that of the traditional algorithm, indicating that achieving area equilibrium to some extent sacrifices the smoothness of the curve. However, the results shown in Fig. 9 are not based on energy constraints. In actual wind power smoothing processes, due to the limited energy of energy storage, the proposed algorithm can achieve better wind power smoothing effects than the traditional EMD algorithm.

B. Comparison of Different Strategies in Smoothing Wind Power Fluctuations

In this subsection, the wind power smoothing performance of the proposed strategy is evaluated.

The case study selects the actual wind power curve of a wind farm in east China, as shown in Fig. 10. The wind farm is equipped with an ESS to smooth wind power fluctuations, with maximum charging/discharging power of 16 MW and rated energy storage capacity of 30 MWh. To ensure the safe operation of the battery, the allowable state-of-charge (SOC) range is set to be 10%-90%. It is assumed that the battery is constrained by the maximum/minimum allowed energy levels during the wind power smoothing process. For comparative analysis, the following strategies are considered.

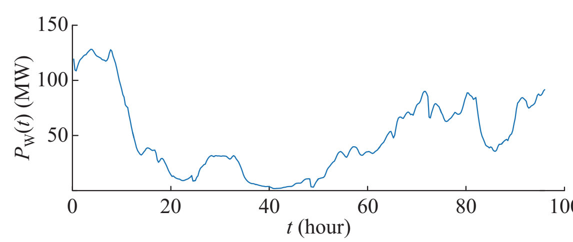

Fig. 10. Actual wind power curve.

Strategy 1: averaging method [10]. Using the average value of wind power as a baseline, the portions above or below the average are used as control commands for the charging and discharging power of energy storage.

Strategy 2: wavelet method [13]-[15]. The wind power is decomposed into wavelet components, and the sum of the first two layers of the wavelet decomposition is used as the control command for the charging and discharging power of energy storage.

Strategy 3: traditional EMD algorithm [23]-[27]. The traditional EMD algorithm is used to decompose the wind power, and the sum of the first two IMFs after decomposition is used as the control command for the charging and discharging power of energy storage.

Strategy 4: the proposed strategy. The proposed strategy is used to decompose the wind power, and the sum of the first two IMFs after decomposition is used as the control command for the charging and discharging power of energy storage.

Figure 11 shows the IMFs $c_1(t)$, $c_2(t)$ obtained by decomposing the wind power $P_W(t)$ using Strategy 4. As can be observed, the modified IMFs $c_1'(t)$ and $c_2'(t)$ have more balanced upper and lower areas, and the integrals of $c_1'(t)$ and $c_2'(t)$ exhibit smaller amplitudes. This indicates that the energy required to smooth the wind power fluctuations using Strategy 4 is lower, which is consistent with the conclusions drawn from Figs. 7 and 8.

Then, the wind power smoothing performance of each strategy is compared. The wind power after smoothing by the energy storage is denoted as $P_L(t)$. To further quantitatively measure the wind power smoothing effects of the four strategies, the smoothness index M_L is calculated using the smoothed wind power $P_L(t)$, which is expressed as:

$$M_L \approx \frac{1}{n_k - 1}\sum_{k=2}^{n_k}\left(\frac{P_L(t_k) - P_L(t_{k-1})}{\Delta t}\right)^2 \tag{23}$$

where n_k is the number of sampling points. A smaller M_L value indicates a higher degree of smoothness.

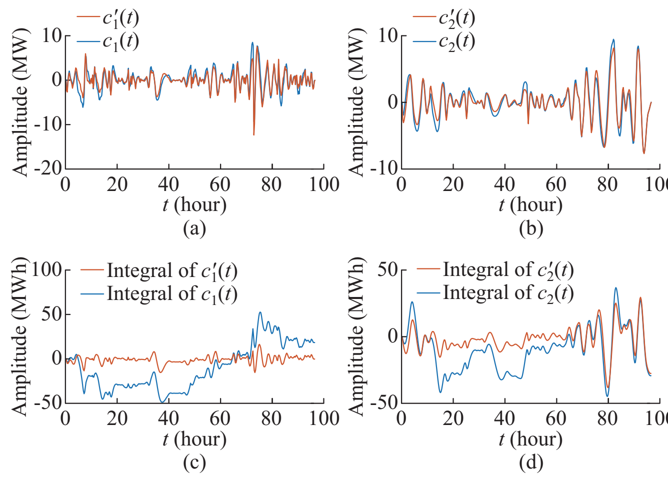

Fig. 11. Wind power decomposition results using Strategy 4. (a) Decomposition results of first IMF ($c_1(t)$ and $c_1'(t)$). (b) Decomposition results of second IMF ($c_2(t)$ and $c_2'(t)$). (c) Integral of first IMF ($c_1(t)$ and $c_1'(t)$). (d) Integral of second IMF ($c_2(t)$ and $c_2'(t)$).

The $P_{ESS}(t)$, ESS energy $E_{ESS}(t)$, and the wind power before and after smoothing for the four strategies are shown in Fig. 12. The calculation results of M_L and the total processing time of the four strategies are listed in Table II.

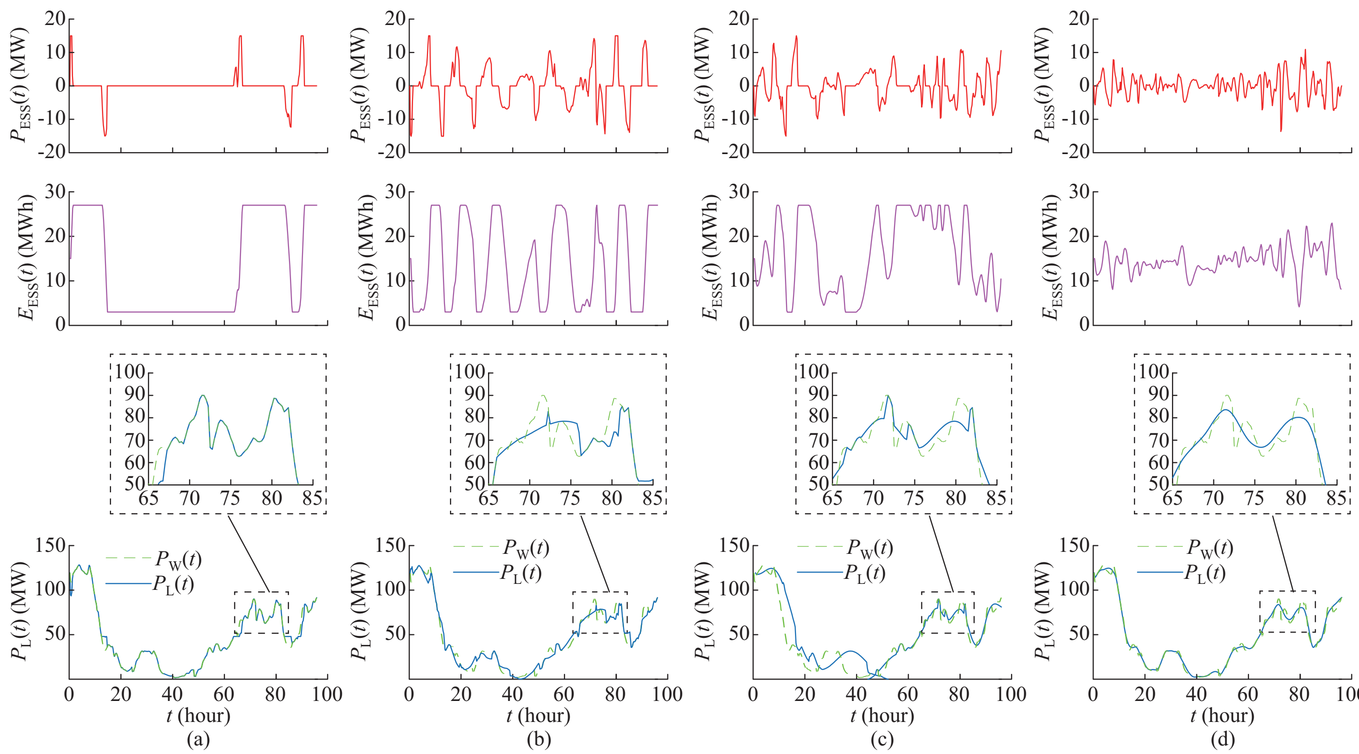

Fig. 12. Comparison of wind power smoothing performances of different strategies. (a) Strategy 1. (b) Strategy 2. (c) Strategy 3. (d) Strategy 4.

TABLE II
CALCULATION RESULTS OF SMOOTHNESS INDEX OF FOUR STRATEGIES

Strategy	M_L (MW^2/h^2)	Computation time (s)
Without smoothing	99.42	
1	138.07	0.0002
2	87.00	1.2264
3	66.09	0.5633
4	35.54	1.8757

1) From the curves of $P_{ESS}(t)$ and $E_{ESS}(t)$ in Fig. 12, it can be observed that compared with the other three strategies, the proposed strategy achieves more balanced upper and lower areas in the $P_{ESS}(t)$ curve and smaller fluctuations in the corresponding $E_{ESS}(t)$ curve. Throughout the entire time window, $E_{ESS}(t)$ of Strategies 1-3 reaches its limit, while Strategy 4 effectively maintains the $E_{ESS}(t)$ within the limit.

2) From the wind power curves before and after smoothing in Fig. 12, it can be observed that while Strategies 1-3 achieve some smoothing effects on the wind power, they are unable to achieve effective smoothing during part of the scheduling periods due to $E_{ESS}(t)$ reaching its limit. In contrast, Strategy 4 achieves excellent smoothing effects throughout the entire time window, significantly outperforming Strategies 1-3. From the smoothness index M_L in Table II, it can be observed that M_L of Strategy 4 is significantly lower than that of Strategies 1-3, indicating better wind power smoothing performance.

3) By comparing the computation time of the four strategies (shown in Table II), it can be observed that Strategy 4 requires the longest computation time among the four strategies, with a computation time more than three times that of Strategy 3. This is because Strategy 4 introduces the area-equilibrium method, which increases the computational load. However, since the total computation time for the 96-hour time window is only 1.8757 s, it is still able to meet the requirements of practical applications.

It should be noticed that Strategy 4 indeed cannot guarantee that the computed upper and lower areas of the IMFs are strictly equal. This is because, when the new dividing line $b_i(t)$ is calculated, it is assumed that $b_i(t)$ is a straight line within the segmented upper and lower areas. In practice, however, $b_i(t)$ is generated using cubic spline or Hermite interpolation, which is not a strictly straight line. Therefore, there exists error in the calculation of the modified IMF, leading to the computed upper and lower areas of the IMFs not being strictly equal.

Nevertheless, even though the upper and lower areas of the IMFs are not strictly equal, Strategy 4 can significantly reduce the area difference between the upper and lower areas of the IMFs. This, in turn, reduces the integrated amplitudes of the IMFs, allowing the strategy to achieve better wind power smoothing performance when the energy storage capacity of the ESS is limited.

C. Wind Power Smoothing Performance in Different Wind Scenarios

In this subsection, the wind power smoothing performance in different wind scenarios is analyzed. The wind power data are sourced from public renewable energy data [29]. The wind farm site 6 with nominal capacity of 96 MW is selected for analysis. Three typical scenarios are selected from the annual wind power data: a high fluctuation scenario, a low wind power scenario, and a high wind power scenario. The high fluctuation scenario uses spring wind power data from April 2 to April 5, 2020; the low wind power scenario uses summer wind power data from August 24 to August 27, 2020; and the high wind power scenario uses winter wind power data from December 3 to December 6, 2020. The parameters for energy storage are assumed to be the same as in the previous subsection.

The proposed strategy is applied to control the charging and discharging power of the ESS so as to smooth wind power fluctuations, and the results are shown in Fig. 13. From Fig. 13, it can be observed that the proposed strategy effectively smoothes wind power fluctuations in all three scenarios, further validating the performance of the proposed strategy.

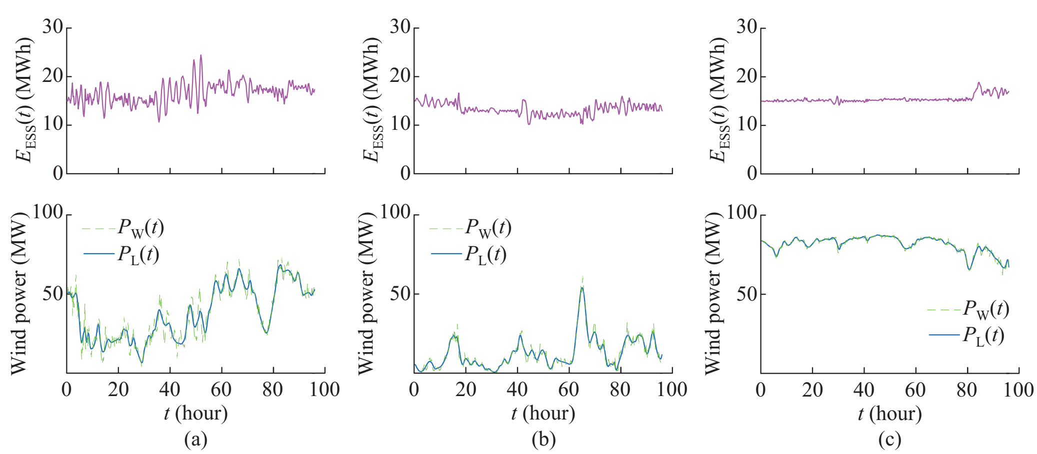

Fig. 13. Wind power smoothing performance in different wind scenarios. (a) Scenario 1. (b) Scenario 2. (c) Scenario 3.

V. Conclusion

This paper proposes a strategy based on the area-equilibrium EMD for smoothing wind power by energy storage, which balances the upper and lower areas of the IMFs obtained through the EMD, thereby minimizing the required energy storage capacity.

Compared with existing strategies, the proposed strategy achieves better wind power smoothing performance. The key findings are as follows.

1) The proposed strategy results in more balanced upper and lower areas of the IMFs obtained through the EMD, with smaller integrated amplitudes of the IMFs and less contained energy.

2) The proposed strategy can smooth wind power output while keeping the energy storage capacity within a smaller range.

3) The strategy achieves better wind power smoothing performance under given energy storage capacity.

The future work may focus on applying the proposed area-equilibrium method to other signal decomposition algorithms, e. g., EEMD and VMD algorithms, in order to explore new wind power smoothing strategies.

References

[1] Q. Wang, X. Zhang, and D. Xu, "Battery energy storage system planning based on super-resolution source-load uncertainty reconstruction," *IEEE Transactions on Smart Grid*, vol. 15, no. 1, pp. 581-594, Jan. 2024.

[2] X. Li, P. Li, L. Ge *et al*., "A unified control of super-capacitor system based on bi-directional DC-DC converter for power smoothing in DC microgrid," *Journal of Modern Power Systems and Clean Energy*, vol. 11, no. 3, pp. 938-949, May 2023.

[3] S. I. Gkavanoudis, K.-N. D. Malamaki, E. O. Kontis *et al*., "Provision of ramp-rate limitation as ancillary service from distribution to transmission system: definitions and methodologies for control and sizing of central battery energy storage system," *Journal of Modern Power Systems and Clean Energy*, vol. 11, no. 5, pp. 1507-1518, Sept. 2023.

[4] I. Ngamroo, "An optimization of superconducting coil installed in an HVDC-wind farm for alleviating power fluctuation and limiting fault current," *IEEE Transactions on Applied Superconductivity*, vol. 29, no. 2, pp. 1-5, Mar. 2019.

[5] Y. Zhai, J. Zhang, Z. Tan *et al*., "Research on the application of superconducting magnetic energy storage in the wind power generation system for smoothing wind power fluctuations," *IEEE Transactions on Applied Superconductivity*, vol. 31, no. 5, pp. 1-5, Aug. 2021.

[6] M. J. E. Alam, K. M. Muttaqi, and D. Sutanto, "Battery energy storage to mitigate rapid voltage/power fluctuations in power grids due to fast variations of solar/wind outputs," *IEEE Access*, vol. 9, pp. 12191-12202, Jan. 2021.

[7] M. Han, G. T. Bitew, S. A. Mekonnen *et al*., "Wind power fluctuation compensation by variable speed pumped storage plants in grid integrated system: Frequency spectrum analysis," *CSEE Journal of Power and Energy Systems*, vol. 7, no. 2, pp. 381-395, Mar. 2021.

[8] Y. Sun, X. Tang, X. Sun *et al*., "Model predictive control and improved low-pass filtering strategies based on wind power fluctuation mitigation," *Journal of Modern Power Systems and Clean Energy*, vol. 7, no. 3, pp. 512-524, May 2019.

[9] Q. Jiang and H. Wang, "Two-time-scale coordination control for a battery energy storage system to mitigate wind power fluctuations," *IEEE Transactions on Energy Conversion*, vol. 28, no. 1, pp. 52-61, Mar. 2013.

[10] X. Shi, Y. Zhao, H. Zhang *et al*., "Control method of wind power fluctuation smoothing for battery energy storage system based on quasi-zero phase filter," *Automation of Electric Power Systems*, vol. 45, no. 4, pp. 45-53, Feb. 2021.

[11] T. Guo, Y. Zhu, Y. Liu *et al*., "Two-stage optimal MPC for hybrid energy storage operation to enable smooth wind power integration," *IET Renewable Power Generation*, vol. 14, no. 13, pp. 2477-2486, Oct. 2020.

[12] X. Wang, J. Zhou, B. Qin *et al*., "Coordinated power smoothing control strategy of multi-wind turbines and energy storage systems in wind farm based on MADRL," *IEEE Transactions on Sustainable Energy*, vol. 15, no. 1, pp. 368-380, Jan. 2024.

[13] Q. Jiang and H. Hong, "Wavelet-based capacity configuration and coordinated control of hybrid energy storage system for smoothing out wind power fluctuations," *IEEE Transactions on Power Systems*, vol. 28, no. 2, pp. 1363-1372, May 2013.

[14] X. Qi, X. Zheng, X. Wang *et al*., "Improved wavelet packet method of smoothing wind power fluctuations based on time-frequency analysis," *Acta Energiae Solaris Sinica*, vol. 43, no. 7, pp. 302-309, Jul. 2022.

[15] T. Guo, Y. Liu, J. Zhao *et al*., "A dynamic wavelet-based robust wind power smoothing approach using hybrid energy storage system," *International Journal of Electrical Power & Energy Systems*, vol. 116, p. 105579, Mar. 2020.

[16] W. Qian, C. Zhao, C. Wan *et al*., "Probabilistic forecasting based stochastic optimal dispatch and control method of hybrid energy storage for smoothing wind power fluctuations," *Automation of Electric Power Systems*, vol. 45, no. 18, pp. 18-27, Sept. 2021.

[17] C. Wan, W. Qian, C. Zhao *et al*., "Probabilistic forecasting based sizing and control of hybrid energy storage for wind power smoothing," *IEEE Transactions on Sustainable Energy*, vol. 12, no. 4, pp. 1841-1852, Oct. 2021.

[18] K. B. Thapa and K. Jayasawal, "Pitch control scheme for rapid active power control of a PMSG-based wind power plant," *IEEE Transactions on Industry Applications*, vol. 56, no. 6, pp. 6756-6766, Nov. 2020.

[19] Y. Ren, P. N. Suganthan, and N. Srikanth, "A novel empirical mode decomposition with support vector regression for wind speed forecasting," *IEEE Transactions on Neural Networks and Learning Systems*, vol. 27, no. 8, pp. 1793-1798, Aug. 2016.

[20] O. Abedinia, M. Lotfi, M. Bagheri *et al*., "Improved EMD-based complex prediction model for wind power forecasting," *IEEE Transactions on Sustainable Energy*, vol. 11, no. 4, pp. 2790-2802, Oct. 2020.

[21] Y. Wu, C. Huang, S. Wu *et al*., "Deterministic and probabilistic wind power forecasts by considering various atmospheric models and feature engineering approaches," *IEEE Transactions on Industry Applications*, vol. 59, no. 1, pp. 192-206, Jan. 2023.

[22] M. Li, Y. Li, and S. S. Choi, "Dispatch planning of a wide-area wind power-energy storage scheme based on ensemble empirical mode decomposition technique," *IEEE Transactions on Sustainable Energy*, vol. 12, no. 2, pp. 1275-1288, Apr. 2021.

[23] X. Lu, Z. Wu, H. Ye *et al*., "Research on hydrogen energy storage to suppress wind power fluctuations based on improved EMD," *Procedia Computer Science*, vol. 224, pp. 365-370, Oct. 2023.

[24] T. Yuan, J. Guo, Z. Yang *et al*., "Optimal allocation of power electric-hydrogen hybrid energy storage of stabilizing wind power fluctuation," *Proceedings of the CSEE*, vol. 44, no. 4, pp. 1397-1405, Feb. 2024.

[25] Y. Chen, P. Jia, G. Meng *et al*., "Optimal capacity configuration of hybrid energy storage system considering smoothing wind power fluctuations and economy," *IEEE Access*, vol. 10, pp. 101229-101236, Sept. 2022.

[26] X. Zheng, F. Bai, Z. Zhuang *et al*., "A novel hierarchical power allocation strategy considering severe wind power fluctuations for wind-storage integrated systems," *International Journal of Electrical Power & Energy Systems*, vol. 153, p. 109363, Nov. 2023.

[27] Y. Zhang, Y. Zhang, and T. Wu, "Integrated strategy for real-time wind power fluctuation mitigation and energy storage system control," *Global Energy Interconnection*, vol. 7, no. 1, pp. 71-81, Feb. 2024.

[28] N. Huang, Z. Shen, S. Long *et al*., "The empirical mode decomposition and the Hilbert spectrum for nonlinear and non-stationary time series analysis," *Proceedings of the Royal Society of London Series A*: *Mathematical*, *Physical and Engineering Sciences*, vol. 454, no. 1971, pp. 903-995, Mar. 1998.

[29] Y. Chen and J. Xu, "Solar and wind power data from the Chinese State Grid Renewable Energy Generation Forecasting Competition," *Scientific Data*, vol. 9, no. 1, pp. 577, Sept. 2022.

Yu-Qing Bao received the Ph. D. degree from Southeast University, Nanjing, China, in 2016, and works as a Faculty Member at Nanjing Normal University, Nanjing, China, since December 2015. His current research interests include power system operation and scheduling, power demand-side management, and frequency control of power systems.

Qing-Quan Yu received the B.S. degree from Nanjing Normal University, Nanjing, China, in 2023. He is currently pursuing the M.S. degree with Nanjing Normal University. His research interests include power system operation and scheduling.

Yu Chen received the B.S. and M.S. degrees from Nanjing Normal University, Nanjing, China, in 2021 and 2024, respectively. His research interests include power system operation and scheduling and power demand-side management.

Shu-Han Yu received the B.S. degree from Nanjing Normal University, Nanjing, China, in 2024. He is currently pursuing the M.S. degree with Nanjing Normal University. His research interests include power system operation and scheduling, power demand-side management, and frequency control of power systems.